ISSN (Print) 1226-1750
ISSN (Online) 2233-6656
Journal of Magnetics 24(1), 190-197 (2019) https://doi.org/10.4283/JMAG.2019.24.1.190

Optimized Design of Improved Permanent Magnet Synchronous Motor for Articulated Robot Using the Penalty Function Method and Response Surface Methodology

Tae-Woo Lee[1], Do-Kwan Hong[1,2]*, and Byung-Chul Woo[2]

[1]*University of Science and Technology, Gyeongsangnam-do 51543, Korea*
[2]*Korea Electrotechnology Research Institute, Gyeongsangnam-do 51543, Korea*

(Received 12 July 2018, Received in final form 6 March 2019, Accepted 11 March 2019)

In this paper, an improved motor is presented for a smart, vertical, multi-joint robot actuator. The motor design was optimized using methodologies such as the penalty function method (PFM) and response surface methodology. To improve its performance, different pole-slot combinations were applied considering its electrical and mechanical characteristics. Using 2D finite element analysis, results were compared from a previous model and a newly proposed model. The experimental results confirmed that the proposed model achieved improved performance at the rated point.

Keywords : Smart actuator, articulated robot, optimized design, penalty function, response surface methodology, pole-slot combination

1. Introduction

Articulated robots have several joints that rotate. Motors cause these to rotate and thus move in the desired direction by exercising motion similar to that in a person's shoulder, arm, elbow, and wrist. These robots have been widely used in industries such as automobiles, electrical/electronic, chemicals, steel, and food. They play a key role in industrial and factory automation [1]. In conventional actuators for these robots, components such as motors, cables, and mechanical parts are separate and connected to each other in complicated ways. Thus, it is very hard to disassemble or reconfigure them. However, if "SMART" actuators are used in robot applications, it is easy to expand various systems through module reconfiguration. The smart actuators have an integral system consisting of a motor, harmonic drive reducer, encoder, controller, and communication board inside the frame. Normally, a hollow shaft is used in a smart actuator for articulated robots because it can save space and extend the lifetime of cables by running them within the shaft where they are protected [2, 3]. The Korea Electrotechnology Research Institute (KERI) had developed a 16-pole, 18-slot surface- mounted permanent magnet synchronous motor (SPMSM) for a smart actuator with reference to UR10 base and shoulder module motor (10-pole, 12-slot). UR10 was developed by Universal Robots and can handle payloads up to 10 kg, as shown in Fig. 1 [4]. In this paper, the different pole-slot combination (20-pole, 24-slot) was provided to improve the performance while considering the winding factor and forced vibration mode.

*Corresponding author: Tel: +82-55-280-1395
Fax: +82-55-280-1490, e-mail: dkhong@keri.re.kr

This paper was presented at the IcAUMS2018, Jeju, Korea, June 3-7, 2018.

2. Design and Analysis for Optimization

2.1. Selection of pole-slot combination

The SPMSM transfers electromagnetic force by means of magnetic flux between permanent magnets in a rotor and electromagnets in the stator. Therefore, when designing the electric motors, the pole-slot combination must be selected considering electrical and mechanical characteristics such as the winding factor, maximum number of parallel circuits, forced vibration mode, and the cogging torque period. The higher the winding factor is, the greater the electrical performance it can provide because of higher utilization of the magnetic flux between rotor and stator. Unless the SPMSM is an ultra-high-speed

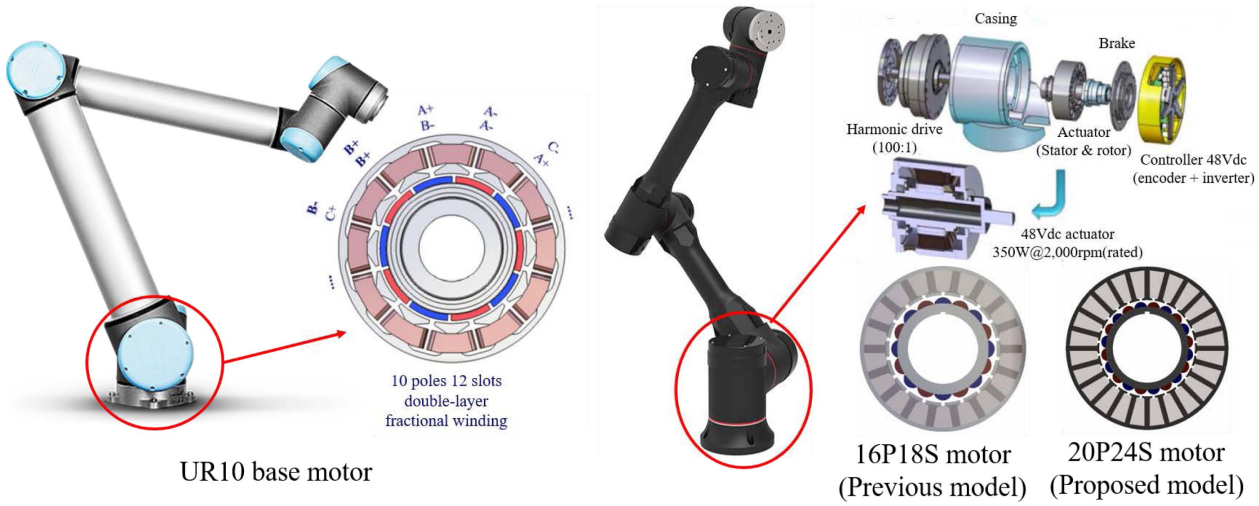

Fig. 1. (Color online) UR10 base motor and KERI's motors in smart actuator.

motor, concentrated winding that is relatively simple and has small end-winding dimensions is used instead of the distributed winding to reduce copper (winding) loss. In addition, the winding within the slot uses double layers to increase utilization. The greatest common divisor (GCD) of the pole-slot combination can be estimated for an approximate mode of the forced vibration. This is because the electromagnetic force from the stator and rotor is most important. The maximum number of parallel circuits can also change performance depending on the combined number of poles and slots. The GCD of the pole-slot combination is also the maximum number of parallel circuits, and in any combination, various parallel circuits can be taken into account. Serial windings and parallel windings have the same characteristics if they are designed based on the same input voltage. However, parallel windings may be considered when the required number of turns cannot be met by the series windings. In addition, whether the winding is parallel or series is often considered in relation to operating speed. This is because series winding is likely to double the operating speed [4].

Because articulated robots perform certain tasks repeatedly in confined spaces, tool position accuracy and repeatability are very important factors. Hence, the 20-pole, 24-slot combination was chosen because it is more stable in terms of vibration because it has higher forced vibration mode than KERI's previous model (16-pole, 18-slot). In Table 1, UR10 base module motor, KERI's previous motor, and newly proposed motor are compared.

Table 1. The comparison of three motors for base module according to pole-slot combination.

Parameters \ Models	10P12S (UR10)	16P18S (KERI)	20P24S (KERI)
Winding factor	0.933	0.945	0.933
Forced vibration mode	2	2	4
Maximum parallel circuit	2	2	4

2.2. Optimization procedure

First, to proceed with the optimal design shown in Fig. 2, four design variables (tooth width (TW), slot opening (SO), thickness of permanent magnet (TPM), and air gap) affecting the shape of the motor, and four design variables (current density (CD), coil outer diameter (OD), number of wire turns, and number of strands) related to the electrical performance were selected, as shown in Fig. 3. Based on the required design specifications in Table 2, an objective function (output torque) and constraint functions (torque constant, torque ripple ratio, and efficiency) were selected. The optimal design criteria were as follows:

$$\text{Maximize: } f(x) \tag{1}$$

Subject to:

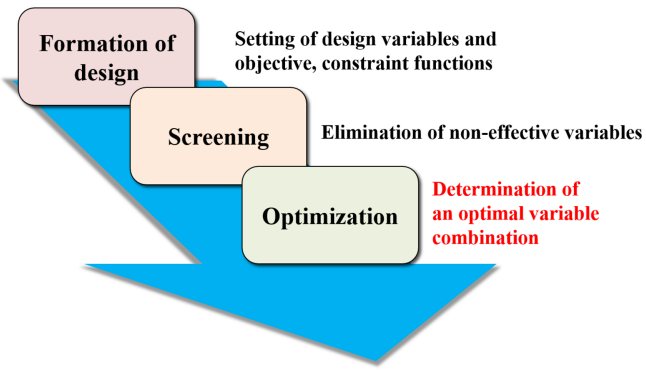

Fig. 2. (Color online) The procedure of optimization design.

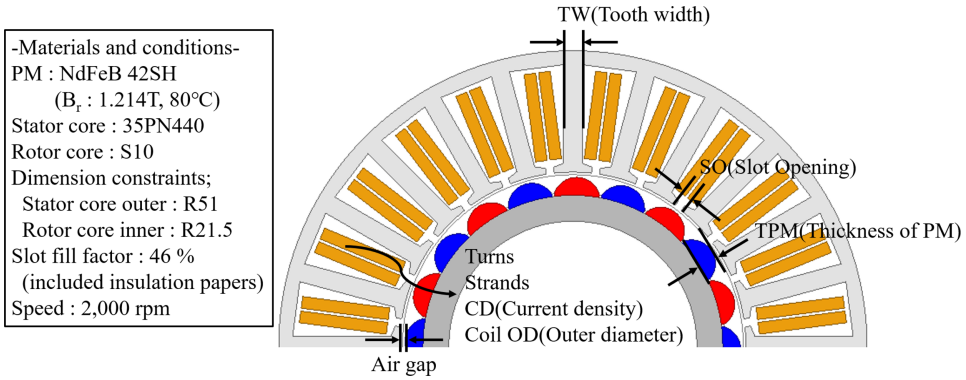

Fig. 3. (Color online) Design variables for 20P24S motor.

Table 2. Required specification for the improved motor.

Parameters \ Models	16P18S	20P24S
DC voltage (V)	48	48
Rated speed (rpm)	2,000	2,000
Output torque (Nm)	1.65	1.8
Torque constant (Nm/A_{rms})	≥ 0.145	≥ 0.145
Torque ripple ratio (%)	≤ 1	≤ 1
Efficiency (%)	≥ 92	≥ 92

$$\begin{cases} \dfrac{g_{ref}(x)}{g(x)} - 1 \le 0 \\ \dfrac{h(x)}{h_{ref}(x)} - 1 \le 0 \quad 0 \\ \dfrac{k_{ref}(x)}{k(x)} - 1 \le 0 \end{cases} \tag{2}$$

Where $f(x)$ denotes output torque and $g(x)$, $h(x)$, and $k(x)$ are torque constant, torque ripple ratio, and efficiency according to design variables x. Here, $g_{ref}(x)$, $h_{ref}(x)$, and $k_{ref}(x)$ indicate references for required specifications (i.e., 0.145 Nm/A_{rms}, 1.0 %, and 92 %).

Considering the multiple variables affecting the results, we went through a screening step to identify those variables that have significant impact and to reduce the range of feasible design. In the screening step, a voltage equation was used that shows the relationship between voltage and current based on a motor equivalent circuit. In the case of an electric motor, it is important to select proper winding specifications. This is because the motor itself cannot be driven if the back electromotive force (EMF) voltage is greater than the input voltage. The motor equivalent circuit is shown in Fig. 4 and the motor voltage equation is shown in (3).

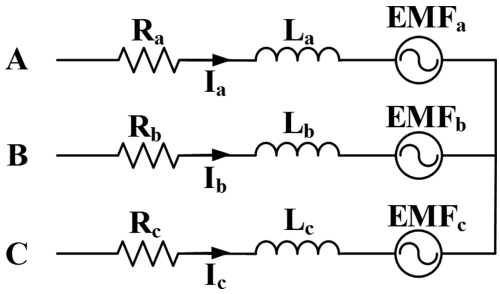

Fig. 4. Equivalent circuit of 3 phase SPMSM.

$$\begin{aligned} V_a &= R_a I_a + L_a \frac{dI_a}{dt} + EMF_a \\ V_b &= R_b I_b + L_b \frac{dI_b}{dt} + EMF_b \\ V_c &= R_c I_c + L_c \frac{dI_c}{dt} + EMF_c \end{aligned} \tag{3}$$

Where V is each phase voltage, R is each phase resistance, I is each phase current, and L is each inductance. Because the inductance values in the voltage equation are smaller than other component values, the voltage margin was calculated by subtracting only EMF voltage and the voltage drop from the input voltage due to the resistance of the winding.

The number of strands was divided into three groups with the two variables (coil O.D, number of wire turns) affecting the windings. In addition, the outer diameter of the coil was reduced by 0.1 mm (from 1 to 0.4 mm) and the number of turns adjusted so that the fill factor of the slot was 46 %, as shown in Table 3. Case 2, which is the highest torque feasible with the required condition area was selected as the initial optimization model, as shown in Fig. 5 [5].

2.2.1. Penalty function method (PFM)

The range of design variables shown in Table 4 is based on previously selected Case 2, and an L18 mixed ortho-

Table 3. Sampling groups in screening step.

Group 1							
Design variables	Case1	Case2	Case3	Case4	Case5	Case6	Case7
Coil O.D (mm)	1.0	0.9	0.8	0.7	0.6	0.5	0.4
Strands	5	5	5	5	5	5	5
Turns	6	8	10	13	18	26	40

Group 2							
Design variables	Case8	Case9	Case10	Case11	Case12	Case13	Case14
Coil O.D (mm)	1.0	0.9	0.8	0.7	0.6	0.5	0.4
Strands	6	6	6	6	6	6	6
Turns	5	6	8	11	15	21	33

Group 3							
Design variables	Case15	Case16	Case17	Case18	Case19	Case20	Case21
Coil O.D (mm)	1.0	0.9	0.8	0.7	0.6	0.5	0.4
Strands	7	7	7	7	7	7	7
Turns	4	5	7	9	12	18	29

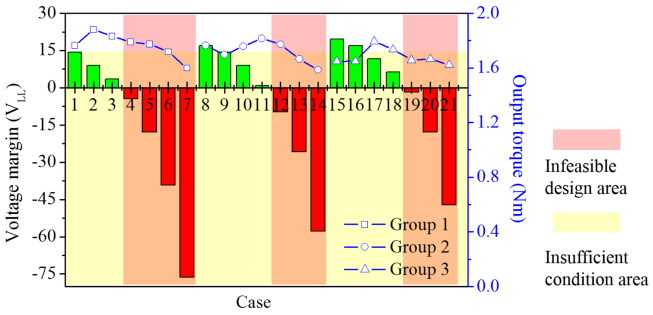

Fig. 5. (Color online) Result of line to line voltage margin and output torque for various case.

gonal array was applied to consider independently the effects of each design variable [6]. The output torque,

Table 4. Level of design variables for L18 mixed orthogonal array.

Design variables		Level 1	Level 2	Level 3
A	CD**	3	4	-
B	Air gap*	0.9	1	1.1
C	TPM*	2.9	3	3.1
D	TW*	3	3.1	3.2
E	SO*	1.4	1.5	1.6
F	Strands	3	4	5
G	Turns	6	7	8
H	Coil OD*	0.8	0.85	0.9

*Unit : (mm), **Unit : (A_{rms}/mm^2)

torque ripple ratio, torque constant, and efficiency were analyzed for 18 cases using 2D finite element analysis (FEA); results of which are shown in Table 5.

The objective function $f(x)$ was previously selected as output torque (1), so it should be maximized when all the constraint conditions are satisfied (2). If the constraints are violated, the penalty functions $p(x)$ defined in (4) will subtract from the objective function. In addition, a quadratic loss function based on the least square method (LSM) was applied to the penalty functions to minimize residuals. To increase accuracy, penalty coefficients α, β, and γ were adjusted within the feasible area. The new characteristic function $\Psi(x)$ by which constraint functions were considered, is shown in (5), where $f_{ref}(x)$ is 1.8 Nm. The main effects analysis result for the new characteristic function is shown in Fig. 6 [8, 9].

$$\begin{cases} p_1(x) = \alpha \times Max(0, \dfrac{g_{ref}(x)}{g(x)} - 1)^2 \\ p_2(x) = \beta \times Max(0, \dfrac{h(x)}{h_{ref}(x)} - 1)^2 \\ p_3(x) = \gamma \times Max(0, \dfrac{k_{ref}(x)}{k(x)} - 1)^2 \end{cases} \tag{4}$$

$$\Psi(x) = \frac{f(x)}{f_{ref}(x)} - \sum_{i=1}^{3} p_i(x) \tag{5}$$

Table 5. L18 mixed orthogonal array with 2D FEA results.

No.	A	B	C	D	E	F	G	H	Torque (Nm)	Torque constant (Nm/A_{rms})	Torque ripple ratio (%)	Efficiency (%)
1	3	0.9	2.9	3	1.4	3	6	0.8	0.514	0.129	4.21	85.150
2	3	0.9	3	3.1	1.5	4	7	0.85	0.919	0.152	0.78	90.104
3	3	0.9	3.1	3.2	1.6	5	8	0.9	1.482	0.174	0.61	92.701
⋮	⋮	⋮	⋮	⋮	⋮	⋮	⋮	⋮	⋮	⋮	⋮	⋮
16	4	1.1	2.9	3.2	1.5	5	6	0.85	1.193	0.119	0.33	91.628
17	4	1.1	3	3	1.6	3	7	0.9	0.939	0.138	0.45	90.284
18	4	1.1	3.1	3.1	1.4	4	8	0.8	1.129	0.160	0.41	91.260

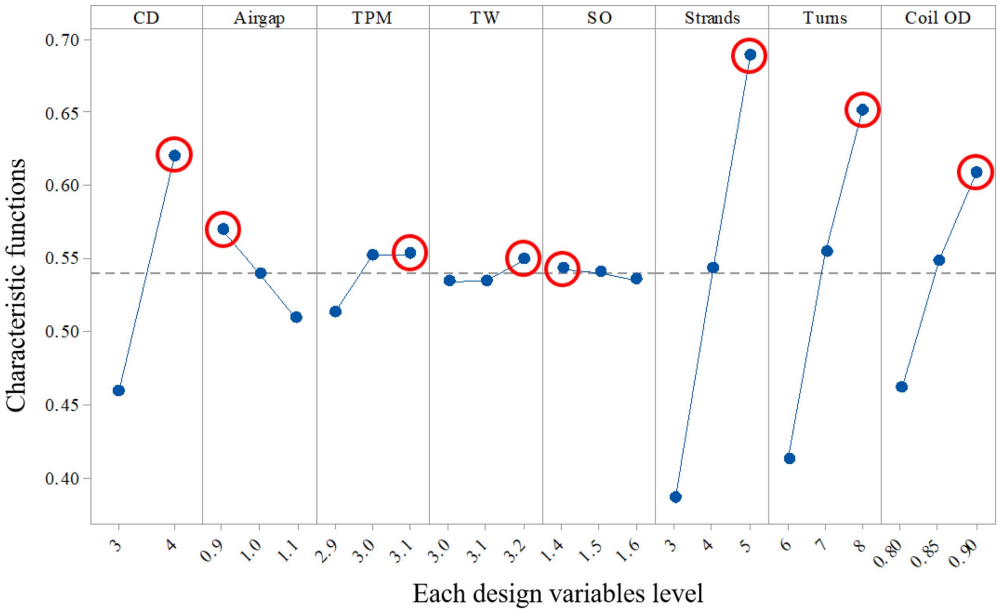

Fig. 6. (Color online) Main effects plot of new characteristic function using penalty functions.

2.2.2. Response surface methodology

The response surface methodology (RSM) is a collection of mathematical and statistical techniques strictly related to the design of experiments (DOE). The main idea is to use the results of the DOE run to create an approximation of the response variable over the design space. The approximation is called a response surface or meta-model (such as a polynomial function) and can be built for any output variable [6, 7, 10]. For appropriate response model estimations, a second-order polynomial model is needed because the output torque, torque constant, and efficiency should be maximized, while torque ripple ratio should be minimized. Moreover, central composite design (CCD) was used in the RSM. The RSM was processed by selecting three highly sensitive variables, the air gap, TPM, and TW (in Fig. 6), all of which, with the exception of variables for the winding specification, have discrete values. The 2D FEA results are shown in Table 6 for 15 cases consisting of 8 vertices, 6 axial points, and 1 center

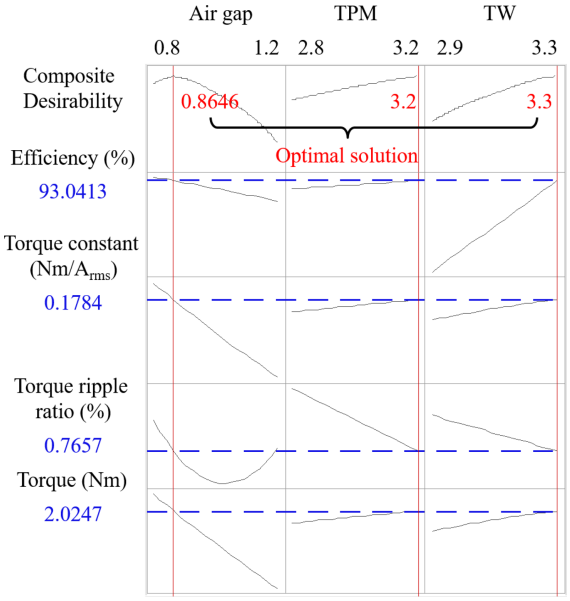

Fig. 7. (Color online) Optimization result of response surface methodology.

Table 6. Central composite design array with 2D FEA results.

No.	Air gap	TPM	TW	Torque (Nm)	Torque constant (Nm/A$_{rms}$)	Torque ripple ratio (%)	Efficiency (%)
1	1.00	2.80	3.10	1.836	0.162	0.56	92.773
2	0.88	3.12	2.98	1.945	0.171	1.23	92.738
3	1.00	3.00	3.10	1.867	0.164	0.64	92.802
⋮	⋮	⋮	⋮	⋮	⋮	⋮	⋮
13	1.00	3.00	3.30	1.884	0.166	0.36	92.988
14	1.12	2.88	3.22	1.774	0.156	0.39	92.858
15	0.80	3.00	3.10	2.024	0.178	2.72	92.858

Table 7. 2D FEA results of previous model and 2 optimized models.

Parameters \ Models	16P18S	PFM	RSM
Space Factor (%)	44.59	46.71	46.95
Coil O.D (mm)	0.9	0.9	0.9
Strands	5	5	5
Turns	8	8	8
Input current (A_{rms})	11.35	11.35	11.35
Current density (A_{rms}/mm^2)	4	4	4
Output Torque (Nm)	1.684	1.968	1.992
Torque ripple ratio (%)	0.32	0.79	0.63
Torque constant (Nm/A_{rms})	0.148	0.173	0.176
Total weight (kg)	1.142	1.077	1.089
Torque density (Nm/kg)	1.474	1.826	1.829
Power density (kW/kg)	0.309	0.383	0.383
Efficiency (%)	92.405	92.931	93.034

point. The results of the optimization using the RSM for the same objective function and constraints are shown in Fig. 7.

The results of optimization using PFM and RSM are shown in Table 7. Table 7 shows that the results of the RSM are better than the optimization results from applying the penalty function, and that the performance has improved compared to the previous model (16-pole, 18-slot) results.

3. Experiment

Based on the final design selected earlier, the motor was fabricated as shown in Fig. 8. Fig. 7 shows the optimization results with an air gap of 0.8646 mm, but the actual air gap chosen was 1 mm to provide a margin considering productivity.

The performance test involved a back-to-back dynamo

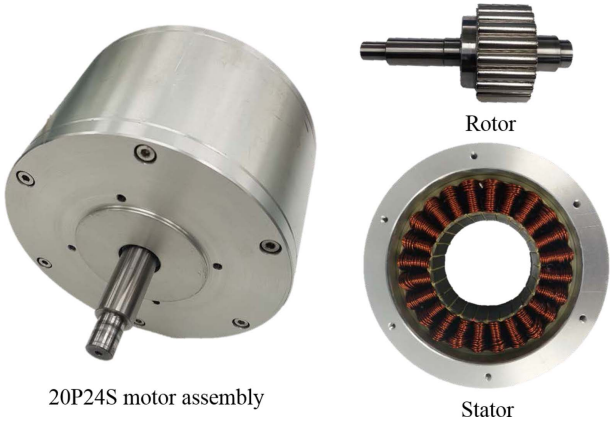

Fig. 8. (Color online) Prototype motor of 20P24S optimal model.

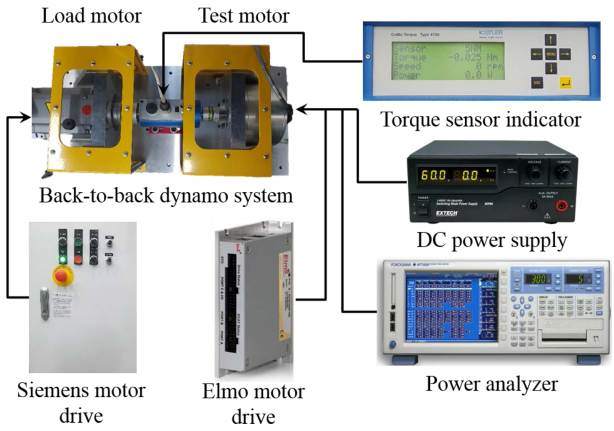

Fig. 9. (Color online) Configuration of performance test equipment.

system with a load motor (Siemens, 1FT7044) and a human machine interface (HMI). The data acquisition system included a power analyzer (Yokogawa, WT1800), a 5 Nm-rated torque sensor (Kistler, 4503B), and the other components shown in Fig. 9 [4].

Before the full load performance test, the back EMF voltage of the test motor was measured and compared with the simulation results by driving the load motors only. Fig. 10 and Table 8 confirmed that the maximum error was 1.18 % at 500 rpm.

In addition, to figure out the mechanical loss of the test motor, only the load motor was operated using speed control in the back-to-back dynamo system. The output power ($L_{ss.total}$) was checked according to the speed when the load motor and the test motor were coupled. Then, only the load motor was driven and the output power ($L_{ss.load}$) was obtained after disconnecting the coupling. If

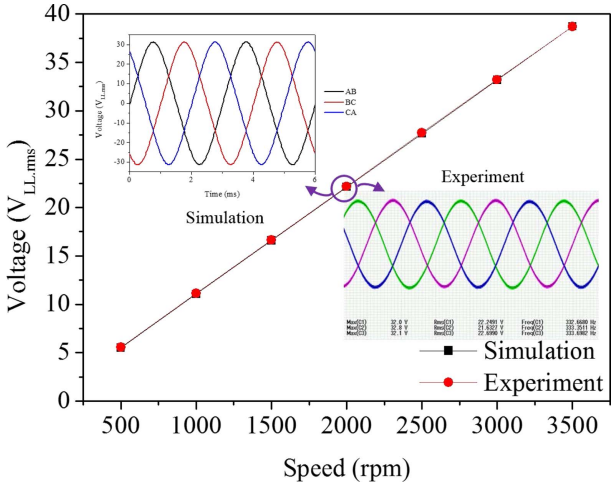

Fig. 10. (Color online) Comparison of the back EMF voltage between simulation and experiment according to increasing speed.

Table 8. Comparison of the back EMF voltage between simulation and experiment.

Parameters \ Speed (rpm)	500	1,000	1,500	2,000	2,500	3,000	3,500
Simulation ($V_{LL.rms}$)	5.53	11.064	16.598	22.118	27.65	33.198	38.706
Experiment ($V_{LL.rms}$)	5.596	11.155	16.667	22.194	27.723	33.22	38.699
Error (%)	1.179	0.812	0.412	0.341	0.264	0.065	0.018

Table 9. Comparison of efficiency with mechanical loss between simulation and experiment at near rated speed.

Speed (rpm) \ Parameters	$L_{ss.total}$ (W)	$L_{ss.load}$ (W)	$L_{ss.test}$ (W)	$L_{ss.iron}$ (W)	$L_{ss.mech}$ (W)	Simul. (%)	Exp. (%)	Error (%)
1,750	19.9	0.3	19.6	15.6	4.0	91.678	89.176	2.729
2,000	24.1	0.3	23.8	18.6	5.2	91.754	89.439	2.523
2,250	28.6	0.4	28.2	21.7	6.5	91.776	89.829	2.122

the two output powers were subtracted, the loss of the test motor ($L_{ss.test}$) including the mechanical loss ($L_{ss.mech}$), and the iron loss ($L_{ss.iron}$) affected by the frequency component for the test motor, could be obtained. The actual mechanical loss of the test motor was calculated by subtracting additional core loss obtained by simulation. The results of the experiment for efficiency and simulation reflected in the actual mechanical loss for efficiency, near the rated speed most commonly used during operation, are shown in Table 9. Comparing the test results with the simulation

Table 10. Elmo drive 1.6 kW Gold DC Whistle specification.

Items	Value	Unit
Minimum supply voltage	12	V_{DC}
Nominal supply voltage	85	V_{DC}
Maximum supply voltage	95	V_{DC}
Maximum continuous power output	1,600	W
Amplitude sinusoidal/DC continuous current	20	A
Sinusoidal continuous RMS current limit (I_c)	14.1	A_{rms}
Peak current limit	$2 \times I_c$	A_{peak}

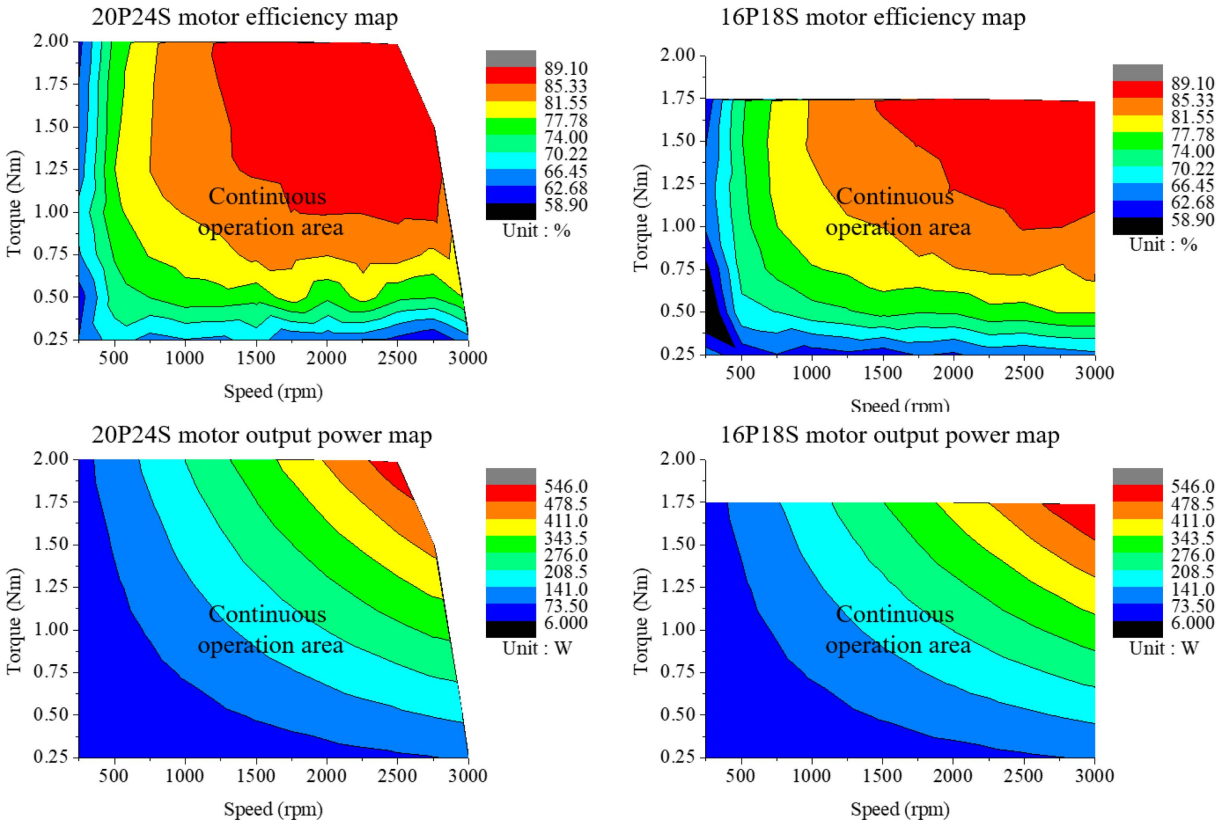

Fig. 11. (Color online) Performance maps for 20P24S and 16P18S motors under current density 4 A/mm^2 and same motor drive.

efficiency considering the actual mechanical loss near the rated speed most commonly used during operation, the average error is about 2.46 %.

For the full load performance test, 48 V_{DC} was supplied to the commercial motor drive (ELMO) and the current was limited due to motor drive specification as shown in Table 10. Therefore, the test was conducted to the area under the rated point (below 4 A/mm^2 current density) where continuous operation is possible. The parameters of the ELMO drive were identical when used in the tests on the previous model (16-pole, 18-slot) and the proposed model (20-pole, 24-slot) under the same conditions. The results on performance map are shown in Fig. 11. Comparing the rated torque at the rated speed as in the 2D FEA results, the proposed motor design has higher torque and greater output power than the previous model at the rated point with same current.

4. Conclusions

In this paper, the optimized design of the motor used in an articulated robot actuator was carried out. After narrowing the design feasible areas through screening, two optimization methods were used to derive an improved model from the previous model. The results of 2D FEA show that the RSM model had higher performance than the optimized model using the penalty function. That is, the torque and torque constants increased by 16.88 % and the efficiency increased by 0.11 % before the optimization process. When the motor from the improved design had been manufactured and tested under the same conditions as the previous model, the newly proposed 20-pole, 24-slot motor had wider operation area (up to 2,500 rpm) than the 16-pole, 18-slot motor. Moreover, comparing the test results with the simulation efficiency considering the actual mechanical loss near the rated speed most commonly used during operation, the result shows an average error of about 2.46 %. In the future, we will also conduct performance tests and noise and vibration evaluations using a drive that has a wide range of current and voltage.

Acknowledgment

This work was supported by the Korea Electrotechnology Research Institute Primary Research Program of MSIP/NST under Grant 18-12-N0101-25.

References

[1] M. Keller, S. Müller, and N. Parspour, 2016 International Symposium on Power Electronics, Electrical Drives, Automation and Motion (SPEEDAM), 849 (2016).
[2] Chan-Hun Park, Jin-Ho Kyung, and Tae-Yong Choi, 2011 11th International Conference on Control, Automation and Systems, 1868 (2011).
[3] Ki-Chang Lee, Ji-Young Lee, Byung-Chul Woo, Jeong-Wook Lee, Young-Jin Lee, and Syung-Kwon Ra, 2018 International Conference on Information and Communication Technology Robotics (ICT-ROBOT), 1 (2018).
[4] Do-Kwan Hong, Wook Hwang, Ji-Young Lee, and Byung-Chul Woo, IEEE Trans. Magn. **54**, 1 (2018).
[5] Tae-Woo Lee, Joon-Woo Mo, Do-Kwan Hong, and Byung-Chul Woo, Trans. Korean Soc. Mech. Eng. A, **42**, 631 (2018).
[6] J. Zhu, S. Li, D. Song, Q. Han, J. Wang, and G. Li, IET Electric Power Applications **12**, 1390 (2018).
[7] S. Ahmed, T. Koseki, and H. Kim, 2018 21st International Conference on Electrical Machines and Systems (ICEMS), 1777 (2018).
[8] Do-Kwan Hong, Byung-Chul Woo, Jung-Hwan Chang, and Do-Hyun Kang, IEEE Trans. Magn. **43**, 1613 (2007).
[9] Jong-Rib Ha, Jae-Gwang Lee, Yeon-Chin Ean, Sang-Ryong Lee, and Hak Yi, 2018 18th International Conference on Control, Automation and Systems (ICCAS) 1723 (2018).
[10] M. Cavazzuti, 1st ed., Springer Science & Business Media 21 (2013).